The local-global multigrid algorithm.

(0) Start
  - $g^L := -K_i^L V_m^L$
  - Prepare an initial guess $\{\phi^L, \phi^G\}$ such that $\phi^L = I_G^L \phi^G$ on Γ_{LG}

(1) Global mesh correction
  - Compute the residual on the local mesh $r^L := g^L - K^L \phi^L$ on $\Omega^L \backslash \Gamma_P$
  - Inject the local mesh solution $\phi^G := \hat{I}_L^G \phi^L$ on Ω_i^G
  - Store ϕ^G in another vector $\hat{\phi}^G := \phi^G$
  - Compute the right-hand side $g^G := K_L^G \hat{\phi}^G + I_G^{L^T} r^L$
  - Compute an approximation for $K^G \phi^G = g^G$
    with the fixed boundary values on Γ_P
  - Correction with the interpolation $\phi^L := \phi^L + I_G^L(\phi^G - \hat{\phi}^G)$ on Ω^L

(2) Smoothing on the local mesh
  - Relax the interior components of ϕ^L for $K^L \phi^L = g^L$
    with the fixed boundary values on $\Gamma_{LG} \cup \Gamma_P$

FIG. 3.1. *The local-global multigrid algorithm.*

Based on the idea proposed by Brandt [2], we add $K_L^G \phi^G$ to both sides of (2.30). Then we obtain the following equations equivalent to (2.29) and (2.30).

$$(3.4) \qquad K^L \phi^L = -K_i^L V_m^L \text{ on } \Omega^L \backslash (\Gamma_{LG} \cup \Gamma_P),$$

$$(3.5) \qquad \lambda = -K^L \phi^L - K_i^L V_m^L \text{ on } \Gamma_{LG},$$

$$(3.6) \qquad K^G \phi^G = I_G^{L^T} \lambda + K_L^G \phi^G \text{ on } \Omega^G \backslash \Gamma_P.$$

If we define the residual vector r^L on the local mesh from (3.4), not only on $\Omega^L \backslash (\Gamma_{LG} \cup \Gamma_P)$, but also on Γ_{LG} by

$$(3.7) \qquad r^L = -K_i^L V_m^L - K^L \phi^L \text{ on } \Omega^L \backslash \Gamma_P,$$

we see that it is identical to the Lagrange multiplier on Γ_{LG} from (3.5).

$$(3.8) \qquad \lambda = r^L \text{ on } \Gamma_{LG}.$$

The above consideration naturally leads to the local-global solution process, shown in Figure 3.1, where (1) and (2) are iterated. Here, the injection $\hat{I}_L^G$ is performed by injecting the local mesh nodal values into the global mesh nodes on Ω_L^G. Note that the correction with the interpolation is also performed on the interface Γ_{LG} in the global mesh correction phase. Thus, together with the assumption on the initial guess, the constraint condition in (2.20) is always satisfied. As for the relaxation on the local and global meshes, a multigrid V-cycle can be applied. In particular, for the local mesh relaxation, one V-cycle is sufficient to smooth the error with respect to the global mesh resolution, where the coarsest mesh of the V-cycle on the local mesh has the same spatial resolution as the global mesh in our implementation, as depicted in Figure 3.2.

The local-global multigrid algorithm obtained above is similar to the multilevel adaptive technique (MLAT) proposed by Brandt [2]. However, MLAT was described for finite difference or finite volume discretizations [20] and derived from the full
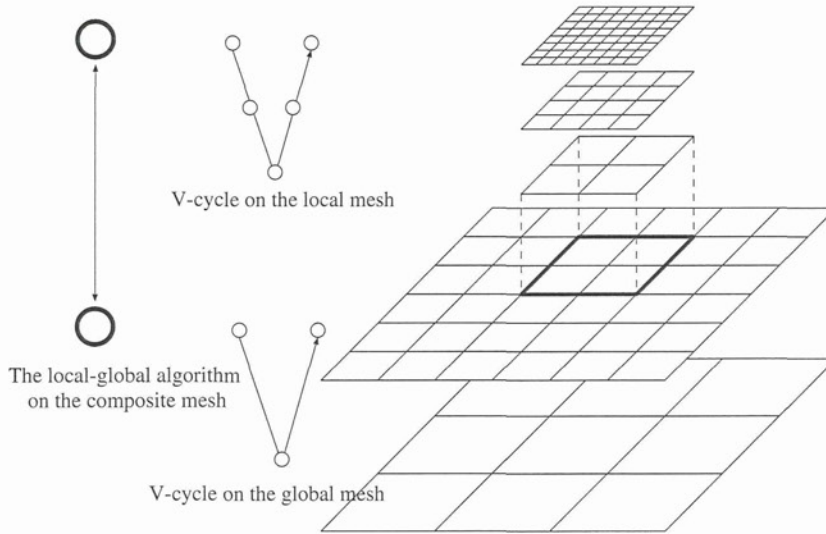
FIG. 3.2. *A sketch of the local-global multigrid algorithm. In each mesh, the multigrid V-cycle is applied as a smoother. In particular, the coarsest grid of the local mesh V-cycle has the same resolution as the finest global mesh.*

approximation scheme (FAS) [2, 20], originally proposed to solve a nonlinear problem with a multigrid. An interesting point here is that MLAT is naturally derived by extending the Lagrange multiplier in (3.6) at the local-global interface Γ_{LG} to the inside of the fine finite element mesh where it can be interpreted as the residual. Also note that in the standard implementation of MLAT [20], the residual at the fine grid boundary is not transferred to the coarse grid, whereas in the above algorithm the residual components at the local mesh interface boundaries certainly affect the right-hand side of the coarse mesh equation. As we have seen in section 2.3, this is an essential point to ensure the conservation property at the local-global interface. Other techniques to ensure the conservation have been introduced, for example, in [1, 12, 27] for finite volume discretizations. On the other hand, in common adaptive finite element approaches, a special refinement strategy is adopted at the fine-coarse interface so that hanging nodes are not present. In these approaches, conservation is automatically ensured. However, a method that allows hanging nodes provides easier mesh generation, in particular, for hexahedral elements.

3.2. Treatment of the Purkinje fiber network. In this section, we describe the special treatment of the Purkinje fibers in the local-global multigrid algorithm. As mentioned in section 1, the Purkinje network is modeled by one-dimensional elements, as is commonly done in the cardiovascular literature. In our simulator, only end-point nodes of the Purkinje network are connected to the voxel mesh nodes, as shown in Figure 3.3(a). Although a fairly fine spatial resolution is required for the Purkinje one-dimensional elements, we can eliminate most of the unknowns before solving the potential problem. This situation is illustrated in Figure 3.3. Nodes on the Purkinje network with only two edges connected can be eliminated without increasing the number of edges. Therefore, we do not apply any coarsening to the matrix on the reduced Purkinje nodes when constructing the matrix at the coarse level. In this case, although we have to invert the matrix completely on the reduced Purkinje nodes at the smoothing steps at each level of the multigrid cycle, this does not result in a
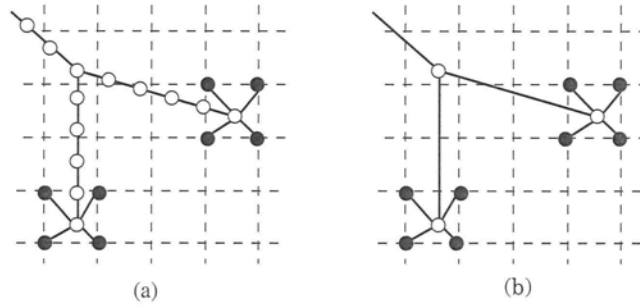
FIG. 3.3. *Original Purkinje network* (a) *and the network after the elimination* (b). *Black nodes are shared nodes with the voxel mesh.*

crucial overhead due to the smaller size of the matrix on the reduced Purkinje nodes.

Here, we show how to construct the matrix on the global mesh for the reduced Purkinje network. In the following, the subscript letters "s" and "r" represent shared nodes and reduced Purkinje nodes, respectively. We assume that the shared nodes are included in the local voxel mesh nodes. Under this notation, a vector $\tilde{\phi}^L$ on the local mesh (involving the reduced Purkinje nodes) is represented as

$$(3.9) \qquad \tilde{\phi}^L = \left[\begin{array}{c} \phi^L \\ \phi_{\mathrm{r}}^L \end{array} \right].$$

According to the above block representation, the coefficient matrix on the local mesh is then represented by

$$(3.10) \qquad \tilde{K}^L = \left[\begin{array}{cc} K^L + D_{\mathrm{s}} & K_{\mathrm{sr}} \\ K_{\mathrm{rs}} & K_{\mathrm{rr}} \end{array} \right].$$

Here, the matrices D_{s}, K_{sr}, K_{rs}, and K_{rr} originate from the reduced stiffness matrices on the reduced Purkinje network. In order to construct an appropriate local-global multigrid algorithm, the reduced Purkinje network should also be connected to the global voxel mesh. In our approach, the matrix on the reduced Purkinje network is not coarsened as mentioned above. Thus, the coefficient matrix on the global mesh is given by

$$(3.11) \qquad \tilde{K}^G = \left[\begin{array}{cc} K^G + I_G^{L^T} D_{\mathrm{s}} I_G^L & I_G^{L^T} K_{\mathrm{sr}} \\ K_{\mathrm{rs}} I_G^L & K_{\mathrm{rr}} \end{array} \right].$$

The interpolation $\tilde{I}_G^L$ from the global to local mesh involving the reduced Purkinje nodes is defined by

$$(3.12) \qquad \tilde{I}_G^L = \left[\begin{array}{cc} I_G^L & 0 \\ 0 & I \end{array} \right].$$

Here, I denotes the identity mapping on the reduced Purkinje nodes. Under these matrices and mappings, the local-global multigrid algorithm in section 3.1 can also be performed with the Purkinje fiber network.

3.3. Relaxation of the local-global multigrid algorithm. In this section, we describe some details of the multigrid V-cycle that is applied "as the relaxation"

in the local-global multigrid algorithm. As for the interpolation from the coarse to the fine mesh, we define two different operators, I_c^f and $\acute{I}_c^f$, as follows. For I_c^f, standard weights are chosen, whereby weights for the voxel mesh nodes that are outside Ω are set to zero. Note that the sum of the interpolation weights of I_c^f is not equal to one if one of the neighboring coarse nodes is outside Ω. In the definition of $\acute{I}_c^f$, the weights are adjusted so that their sum is equal to one, except for the fine nodes for which all the neighboring coarse nodes are outside Ω. In our implementation, we apply I_c^f as the interpolation operator and its transpose as the restriction operator in the multigrid V-cycles, whereas in the determination of the coefficient matrix K^c on the coarse mesh from the coefficient matrix K^f on the fine mesh, we apply $\acute{I}_c^f$ as follows.

$$(3.13) \qquad K^c = (\acute{I}_c^f)^T K^f \acute{I}_c^f.$$

In our experience, the above-mentioned strategy (using the different interpolations in the multigrid cycle and in the determination of the coarse mesh matrix) results in the best convergence. For example, using $\acute{I}_c^f$ for both leads to convergence stagnation when the Purkinje fiber network is connected, while using I_c^f for both results in slower convergence. Further study of this is part of our future research.

The other key issue for robust convergence in the given potential problem is the choice of smoother in the multigrid. In this application, the electric conductivity has an anisotropy in the heart muscle along the fabric construction and also jumps in coefficients at the interfaces between different organs. Furthermore, the torso boundaries given on the finest level on the global mesh do not necessarily fit with the coarser voxel elements. These problems trigger convergence difficulties for the standard multigrid method. Therefore, we adopt an incomplete Cholesky (IC) smoother since it is more powerful than a Gauss–Seidel smoother for jumping coefficient and anisotropic problems (see, for example, [20] or [29]). Thus, the coarse mesh correction may be somewhat less accurate. In the case where the Purkinje fiber network is connected, we apply the IC smoother on the voxel part and a sparse direct solution method on the reduced Purkinje network part with the two-block representation as in (3.10). In general, the linear equation to be solved at an arbitrary level can be represented as follows (see (3.11)).

$$(3.14) \qquad \begin{bmatrix} K + I^{sT}D_sI^s & I^{sT}K_{sr} \\ K_{rs}I^s & K_{rr} \end{bmatrix} \begin{bmatrix} \phi \\ \phi_r \end{bmatrix} = \begin{bmatrix} g \\ g_r \end{bmatrix}.$$

Here, K is the coefficient matrix on the grid where the smoother is applied, and I^s denotes the interpolation operator of the shared nodes on the finest local mesh Ω^L from the grid where the smoother is applied. Under the above notation, one smoothing step is described as follows.

$$(3.15) \qquad r^{(k)} = g - (K + I^{sT}D_sI^s)\phi^{(k)} - I^{sT}K_{sr}\phi_r^{(k)},$$

$$(3.16) \qquad \text{Solve } M\Delta\phi^{(k+1)} = r^{(k)},$$

$$(3.17) \qquad \phi^{(k+1)} = \phi^{(k)} + \Delta\phi^{(k+1)},$$

$$(3.18) \qquad r_r^{(k+1/2)} = g_r - K_{rr}\phi_r^{(k)} - K_{rs}I^s\phi^{(k+1)},$$

$$(3.19) \qquad \text{Solve } K_{rr}\Delta\phi_r^{(k+1)} = r_r^{(k+1/2)},$$

$$(3.20) \qquad \phi_r^{(k+1)} = \phi_r^{(k)} + \Delta\phi_r^{(k+1)},$$

where M denotes the IC factorization of the matrix $K + I^{sT}D_sI^s$.

Another important technique to improve robustness is the Krylov subspace acceleration technique. One iteration of the multilevel solution is applied as a preconditioner for the Krylov subspace method. In the case of a composite mesh application, the implementation of a matrix-vector product may require considerable effort. However, as shown in the literature [3, 28], one can obtain a Krylov subspace acceleration by recombining iterants when their residuals are available. Details of our acceleration algorithm for this application are given in Appendix B.

4. Numerical experiments with a realistic torso model and Purkinje fiber network. In this section, we evaluate the performance of the local-global multigrid algorithm for a realistic model on which the real-life simulations described in section 1 are performed. In the model, the voxel mesh data of the organs in Figure 1.5 are prepared based on the Visible Human dataset [25]. The mesh sizes and intervals of the local and global voxel meshes are described in Table 4.1. The ratio of the local and global mesh intervals is equal to 4. An illustration of the Purkinje fiber network adopted in the simulation is depicted in Figure 4.1. The geometry of the network is based on an anatomical observation in [18]. Its conductivity is set to 100 mS/cm, which is much larger than the values in Table 1.1. The conductivity has been adjusted in order to reproduce the experimental observation of excitation propagation given in the literature [7]. The Purkinje-ventricular delay [13] is not taken into account in the current simulation, and the radius of the cross section of the network is set to 0.05 cm except near the interconnection points with the heart muscle where 0.01 cm or 0.03 cm is used. These radius values have also been adjusted in order to reproduce proper excitation conduction from the Purkinje fiber to the ventricular muscle. The total number of Purkinje nodes is 24509, of which 9882 nodes are shared with the local voxel mesh. The number of nonzero components in the matrix on the Purkinje network is 73709. However, after the reduction to the reduced Purkinje nodes, only 3937 nodes are left (besides the shared nodes). Finally, matrix K_{rr} in (3.10) consists of 11989 nonzero components. The sparse LU factorization of matrix K_{rr} has only 16481 nonzeros with a fill-in reduced ordering. Thus, the solution to K_{rr} in (3.19) in the smoother is unlikely to produce a crucial overhead.

TABLE 4.1
Local and global mesh sizes and intervals.

Local mesh		Global mesh	
Size (x, y, z)	Interval length	Size (x, y, z)	Interval length
(288, 288, 368)	0.4 mm	(256, 256, 288)	1.6 mm

As for the relaxation on the local and global meshes, the multigrid V-cycle, with one pre- and one postsmoothing iteration, is applied. The V-cycle on the local mesh consists of three levels as the coarsest local mesh then has the same spatial resolution as the finest global mesh. One smoothing iteration is performed on the coarsest local mesh. The V-cycle on the global mesh consists of six levels. On the coarsest global mesh, twenty smoothing iterations are performed.

First, we examine the parallel performance of the local-global multigrid algorithm. Parallelization strategies used in our implementation are described in Appendix C. The timing results are measured on a PC-cluster composed of Pentium 4 processors (3.2GHz) connected via Myrinet. Shown in Table 4.2 are the elapsed times for the main processes in one iteration of the local-global multigrid algorithm, where the performance was examined for up to 80 processors. In the table, "L to G" and
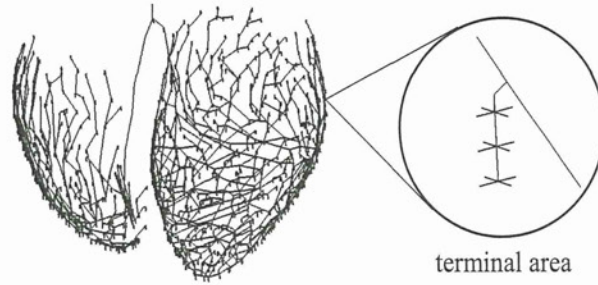
FIG. 4.1. *The Purkinje fiber network. At each terminal, the fiber is attached with 12 shared nodes.*

TABLE 4.2
Elapsed time (in seconds) of one iteration of the local-global multigrid algorithm for the different divisions of the meshes.

Division	L to G	G to L	Krylov	Smoother		Total
				Voxel	Purkinje	
$4 \times 4 \times 2$	0.09 (3.5%)	0.13 (4.9%)	0.12 (4.4%)	0.79 (30.1%)	0.30 (11.5%)	2.62
$4 \times 4 \times 3$	0.07 (3.4%)	0.09 (4.7%)	0.08 (4.4%)	0.56 (29.7%)	0.27 (14.4%)	1.89
$4 \times 4 \times 4$	0.05 (3.4%)	0.07 (4.7%)	0.06 (4.0%)	0.42 (27.8%)	0.22 (14.4%)	1.51
$4 \times 4 \times 5$	0.04 (3.3%)	0.06 (4.5%)	0.05 (3.9%)	0.33 (27.3%)	0.20 (16.1%)	1.22

"G to L" denote the elapsed times for the local-to-global and global-to-local data transformations in (C.1), respectively. "Krylov" denotes the elapsed time for the Krylov acceleration. "Smoother" denotes the elapsed time for the smoothing iterations at all levels, where "Voxel" corresponds to the relaxation on the voxel meshes in (3.16) and (3.17), and "Purkinje" corresponds to the processes on the shared and reduced Purkinje nodes in (3.15), (3.18), (3.19), and (3.20). The numbers in parentheses are the ratios to the total time.

We observe a very satisfactory scaling. The elapsed times for the data transformations between the local and global meshes are relatively small in all cases. However, the elapsed time for the smoothing on the reduced Purkinje nodes is more pronounced as the number of processors increases. In particular, in (3.15) and (3.18), one-to-many communications are necessary to transfer the data to the shared nodes. It seems that this influences the parallel performance negatively.

Further, we analyze the convergence of the local-global multigrid algorithm. The convergence histories with respect to the number of iterations and the elapsed times are presented in Figure 4.2 for three different approaches. The notations "strong coupling with Krylov" and "strong coupling without Krylov" denote the local-global multigrid algorithm, respectively, with and without the Krylov acceleration technique, where the reduced Purkinje nodes are taken into account in the smoothing at every level, as described in section 3.3. On the other hand, the notation "loose coupling with Krylov" denotes the solution algorithm with the Krylov acceleration technique but solving the reduced Purkinje nodes and the voxel nodes in a decoupled way. This means that the direct solution on the reduced Purkinje nodes (including the shared nodes) and the local-global multigrid algorithm on the voxel mesh are performed alternately. In this case, the coupling with the reduced Purkinje nodes is dealt with only at the finest level on the local mesh.
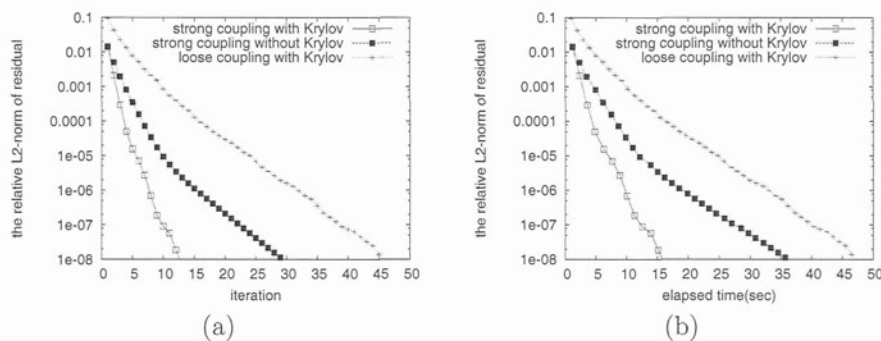
FIG. 4.2. *Convergence history with respect to* (a) *iterations and* (b) *elapsed time.*

In the Krylov acceleration technique, up to five iterants are recombined for the acceleration, and the acceleration, process is restarted every five iterations. The results in Figure 4.2 show the effectiveness of the Krylov acceleration technique and the importance of the smoothing on the reduced Purkinje nodes at every level. The convergence speed of the loose coupling approach is obviously much slower than that of the proposed local-global multigrid algorithm. Even though there is considerable overhead in dealing with the reduced Purkinje nodes at every level, the proposed algorithm is still significantly faster than the loose coupling approach also with respect to the elapsed time. In our real-life simulations, we commonly adopt 10^{-5} as the convergence tolerance for the relative L2-norm of the residual. Therefore, one solution takes approximately 8 seconds. If we solve the potential problem every 1 or 0.2 ms, about 8000 or 40000 seconds, respectively, are needed for the solutions to a 1 second simulation with 80 processors. This is approximately 40 or 70%, respectively, of the total elapsed time in the ECG simulation to obtain the results given in Figure 2.2.

5. Conclusions. A parallel solution to the bidomain equation that appears in the excitation propagation analysis of the human heart was constructed. The stability of the explicit scheme was analyzed and an efficient multigrid technique to solve the potential problem with the torso model was introduced. In our approach, the potential problem was discretized on the composite mesh composed of a fine local mesh around the heart and a coarse global mesh covering the torso. A conservative finite element discretization adopting the Lagrange multiplier approach was introduced and a multigrid solution technique for this discretization was naturally derived. Furthermore, a method to combine the Purkinje fiber network with the multigrid solution technique was shown, whereby the matrix on the Purkinje network was reduced before entering the multilevel solver and the reduced matrix on the network was dealt with by a direct solution method at every level. The parallel efficiency and good convergence results were proved through an experiment with a realistic simulation model.

Appendix A. Stability analysis for the bidomain integration scheme. In order to evaluate the spectral radius of $\mathcal{M}$ in (2.12), we construct a matrix as described below.

LEMMA A.1. *Assume that the spectral radius of $\boldsymbol{D}_{\mathrm{m}}^{-1}\boldsymbol{K}_{\mathrm{i}}$ is less than 1. Then $\mathcal{M}$ in (2.12) is similar to the following matrix.*

$$(A.1) \qquad \mathcal{M} \sim \begin{bmatrix} \boldsymbol{I} - \boldsymbol{S}\boldsymbol{S}^T & -(\boldsymbol{I} - \boldsymbol{S}\boldsymbol{S}^T)^{\frac{1}{2}}\boldsymbol{S}\boldsymbol{T} \\ -\boldsymbol{T}^T\boldsymbol{S}^T(\boldsymbol{I} - \boldsymbol{S}\boldsymbol{S}^T)^{\frac{1}{2}} & \boldsymbol{T}^T\boldsymbol{S}^T\boldsymbol{S}\boldsymbol{T} \end{bmatrix},$$

with

(A.2) $$S = D_{\mathrm{m}}^{-\frac{1}{2}} K_{\mathrm{i}}^{\frac{1}{2}},$$

(A.3) $$T = K_{\mathrm{i}}^{\frac{1}{2}} (K_{\mathrm{i}} + K_{\mathrm{e}})^{-\frac{1}{2}}.$$

Here, I indicates the identity matrices on the subspaces.

Proof. From (2.12), we obtain

$$\mathcal{M} = \begin{bmatrix} D_{\mathrm{m}}^{-1} & 0 \\ -(K_{\mathrm{i}} + K_{\mathrm{e}})^{-1} K_{\mathrm{i}} D_{\mathrm{m}}^{-1} & (K_{\mathrm{i}} + K_{\mathrm{e}})^{-1} \end{bmatrix} \begin{bmatrix} D_{\mathrm{m}} - K_{\mathrm{i}} & -K_{\mathrm{i}} \\ 0 & 0 \end{bmatrix}$$

$$= \begin{bmatrix} I - D_{\mathrm{m}}^{-1} K_{\mathrm{i}} & -D_{\mathrm{m}}^{-1} K_{\mathrm{i}} \\ -(K_{\mathrm{i}} + K_{\mathrm{e}})^{-1} K_{\mathrm{i}} (I - D_{\mathrm{m}}^{-1} K_{\mathrm{i}}) & (K_{\mathrm{i}} + K_{\mathrm{e}})^{-1} K_{\mathrm{i}} D_{\mathrm{m}}^{-1} K_{\mathrm{i}} \end{bmatrix}.$$

By multiplying $\begin{bmatrix} D_{\mathrm{m}}^{\frac{1}{2}} & 0 \\ 0 & (K_{\mathrm{i}} + K_{\mathrm{e}})^{\frac{1}{2}} \end{bmatrix}$ to the left and its inverse to the right, we obtain

(A.4) $$\mathcal{M} \sim \begin{bmatrix} I - SS^T & -ST \\ -T^T S^T (I - SS^T) & T^T S^T ST \end{bmatrix}.$$

By multiplying $\begin{bmatrix} (I - SS^T)^{\frac{1}{2}} & 0 \\ 0 & I \end{bmatrix}$ to the left and its inverse to the right, we obtain (A.1).   □

From the above lemma, we obtain the following relation for the spectral radii.

(A.5) $$\rho(\mathcal{M}) = \rho(\mathcal{N}),$$

with

(A.6) $$\mathcal{N} = \begin{bmatrix} I - SS^T & -(I - SS^T)^{\frac{1}{2}} ST \\ -T^T S^T (I - SS^T)^{\frac{1}{2}} & T^T S^T ST \end{bmatrix}.$$

Note that $\mathcal{N}$ is a symmetric matrix, thus we only need to evaluate its eigenvalues to determine the spectral radius. The following lemma can be applied to the evaluation.

LEMMA A.2. *For an $n \times n$ positive symmetric matrix A and an $n \times m$ matrix B, let us define an $(n + m) \times (n + m)$ matrix $\mathcal{N}(A, B)$ by*

(A.7) $$\mathcal{N}(A, B) \equiv \begin{bmatrix} A^2 & -AB \\ -B^T A & B^T B \end{bmatrix}.$$

Then $\mathcal{N}(A, B)$ has m zero eigenvalues and the nonzero eigenvalues are the same as those of $A^2 + BB^T$.

Proof. For an arbitrary m-dim vector y, we see

(A.8) $$\mathcal{N}(A, B) \begin{bmatrix} A^{-1} B y \\ y \end{bmatrix} = \begin{bmatrix} 0 \\ 0 \end{bmatrix}.$$

Thus, the kernel of $\mathcal{N}(A, B)$ includes at least the m-dim subspace:

(A.9) $$S_1 = \left\{ \begin{bmatrix} A^{-1} B y \\ y \end{bmatrix} \mid y \in R^m \right\}.$$

The orthogonal complement of S_1 is represented as follows.

(A.10) $$S_1^{\perp} = \left\{ \begin{bmatrix} x \\ -B^T A^{-1} x \end{bmatrix} \mid x \in R^n \right\}.$$

Let $\left[\begin{smallmatrix} \boldsymbol{x} \\ -\boldsymbol{B}^T\boldsymbol{A}^{-1}\boldsymbol{x} \end{smallmatrix}\right]$ be an eigenvector in $S_1^{\perp}$ with an eigenvalue λ. Then the following equality must hold.

$$(A.11) \qquad (\boldsymbol{A}^2 + \boldsymbol{A}\boldsymbol{B}\boldsymbol{B}^T\boldsymbol{A}^{-1})\boldsymbol{x} = \lambda\boldsymbol{x}.$$

Here, we have the similarity relation

$$(A.12) \qquad \boldsymbol{A}^2 + \boldsymbol{A}\boldsymbol{B}\boldsymbol{B}^T\boldsymbol{A}^{-1} \sim \boldsymbol{A}^2 + \boldsymbol{B}\boldsymbol{B}^T.$$

Thus, the lemma is shown.   □

From Lemmas A.1 and A.2, we can prove Theorem 2.1 as follows. If $\rho(\boldsymbol{D}_{\mathrm{m}}^{-1}\boldsymbol{K}_{\mathrm{i}}) < 1$, the assumption in Lemma A.1 holds. Thus, if we set $\boldsymbol{A} = (\boldsymbol{I} - \boldsymbol{S}\boldsymbol{S}^T)^{\frac{1}{2}}$, $\boldsymbol{B} = \boldsymbol{S}\boldsymbol{T}$, we obtain

$$(A.13) \qquad \mathcal{M} \sim \begin{bmatrix} \boldsymbol{A}^2 & -\boldsymbol{A}\boldsymbol{B} \\ -\boldsymbol{B}^T\boldsymbol{A} & \boldsymbol{B}^T\boldsymbol{B} \end{bmatrix}.$$

Thus, from Lemma A.2,

$$(A.14) \qquad \rho(\mathcal{M}) = \rho\left(\begin{bmatrix} \boldsymbol{A}^2 & -\boldsymbol{A}\boldsymbol{B} \\ -\boldsymbol{B}^T\boldsymbol{A} & \boldsymbol{B}^T\boldsymbol{B} \end{bmatrix}\right) = \rho\left(\boldsymbol{A}^2 + \boldsymbol{B}\boldsymbol{B}^T\right).$$

Here,

$$(A.15) \qquad \boldsymbol{A}^2 + \boldsymbol{B}\boldsymbol{B}^T = \boldsymbol{I} - \boldsymbol{S}(\boldsymbol{I} - \boldsymbol{T}\boldsymbol{T}^T)\boldsymbol{S}^T,$$

where $\boldsymbol{I} - \boldsymbol{T}\boldsymbol{T}^T$ is nonnegative from the definition of $\boldsymbol{T}$ in (A.3), and $\boldsymbol{S}\boldsymbol{S}^T \sim \boldsymbol{D}_m^{-1}\boldsymbol{K}_{\mathrm{i}}$. Hence, we obtain

$$\rho(\boldsymbol{I} - \boldsymbol{S}(\boldsymbol{I} - \boldsymbol{T}\boldsymbol{T}^T)\boldsymbol{S}^T) \leq 1 - \lambda_{\min}(\boldsymbol{S}(\boldsymbol{I} - \boldsymbol{T}\boldsymbol{T}^T)\boldsymbol{S}^T)$$
$$\leq 1 - \lambda_{\min}(\boldsymbol{S}\boldsymbol{S}^T)\lambda_{\min}(\boldsymbol{I} - \boldsymbol{T}\boldsymbol{T}^T) \leq 1 - \lambda_{\min}(\boldsymbol{S}\boldsymbol{S}^T)(1 - \lambda_{\max}(\boldsymbol{T}\boldsymbol{T}^T)),$$

and (2.15) is proved.

Appendix B. Krylov subspace acceleration technique. Let us assume that we have a linear problem where we only have tools to generate a new improved solution vector $\boldsymbol{u}_{\mathrm{new}}$ from a given old solution vector $\boldsymbol{u}_{\mathrm{old}}$,

$$(B.1) \qquad \boldsymbol{u}_{\mathrm{new}} := \mathrm{Sol}(\boldsymbol{u}_{\mathrm{old}}),$$

and to compute the residual vector $\boldsymbol{r}$ for a given solution vector $\boldsymbol{u}$,

$$(B.2) \qquad \boldsymbol{r} := \mathrm{Res}(\boldsymbol{u}).$$

Let us assume that we have a sequence of $m + 1$-solutions and their corresponding residuals.

$$\boldsymbol{u}_{k+1} = \mathrm{Sol}(\boldsymbol{u}_k), \ k = 0, \ldots, m-1,$$
$$\boldsymbol{r}_k = \mathrm{Res}(\boldsymbol{u}_k), \ k = 0, \ldots, m.$$

We compute an improved solution vector $\tilde{\boldsymbol{u}}$ by recombining the iterants as follows.

$$\tilde{\boldsymbol{u}} = \boldsymbol{u}_m + \sum_{k=1}^{m} \alpha_k(\boldsymbol{u}_k - \boldsymbol{u}_{k-1})$$

$$(B.3) \qquad = (1 + \alpha_m)\boldsymbol{u}_m + \sum_{k=1}^{m-1}(\alpha_k - \alpha_{k+1})\boldsymbol{u}_k - \alpha_0\boldsymbol{u}_0.$$

Since the summation of the coefficients in (B.3) is 1, the residual vector for $\tilde{u}$ is represented by

$$(B.4) \qquad \tilde{r} = \mathrm{Res}(\tilde{u}) = r_m + \sum_{k=1}^{m} \alpha_k (r_k - r_{k-1}).$$

Thus, in order to minimize the norm of $\tilde{r}$, we only need to solve a linear system:

$$(B.5) \qquad \sum_{j=1}^{m} (r_i - r_{i-1}) \cdot (r_j - r_{j-1}) \alpha_j = r_m \cdot (r_i - r_{i-1}), \ i = 1, \dots, m.$$

In order to apply the above acceleration technique, we need to clarify what the residual operator Res in (B.4) is. The constraint condition (2.20) is always satisfied for the solution sequence given by the local-global multigrid algorithm. Thus, we do not need to evaluate the residual components for the constraint conditions. Therefore, we can determine the residual vector by compressing components of the residuals given by (3.4), (3.5), and (3.6).

$$(B.6) \qquad r^L = -K^L \phi^L - K_{\mathrm{i}}^L V_{\mathrm{m}}^L \text{ on } \Omega^L \backslash (\Gamma_{LG} \cup \Gamma_P),$$

$$(B.7) \qquad r^G = -\overline{K_L^G} \phi^G + I_G^{L^T} \lambda \text{ on } \overline{\Omega_L^G} \backslash \Gamma_P,$$

where λ on Γ_{LG} is computed from (3.5).

If rounding errors are not taken into account, the above acceleration technique produces a solution identical to the right-preconditioned GMRES method (see [28]). Typically, the process converges in a small number of iterations with the powerful multigrid preconditioner.

Appendix C. Parallelization strategy. Here, we introduce the parallelization strategy of the bidomain analysis on a distributed memory parallel computer. Figure C.1 depicts the general situation for a composite mesh.

Note that there is no problem regarding the conservation discussed in section 2.3 even in the case where the local voxel mesh covers more than the torso region, as long as the boundaries of the torso on the local mesh coincide with the global mesh edges. In such a case, the local voxel mesh nodes on the torso boundaries are excluded from Γ_{LG}. Thus, there is no exchange of current there.

As shown on the right-hand side of Figure C.1, the solution process is decomposed into three phases with respect to data distribution between the processors. The first phase corresponds to the explicit Euler time integration of the inner iteration described in section 2.1. Here, the computation is performed only at the nodes on the heart muscle Ω_H. The second and third phases include the local-global multigrid algorithm described in section 3.1 on the local and global voxel meshes, respectively. For the second and third phases, the nodes are partitioned regularly in each direction. In contrast, the first phase is based on a partitioning of an unstructured graph which consists of the nodes only on the heart muscle Ω_H. For the partitioning, we adopt the graph partitioning tool ParMETIS [9] to obtain the partitioning information. Since these data distributions are not consistent, as can be seen in Figure C.1, redistribution of variables takes place at each phase change. The variables that are redistributed at
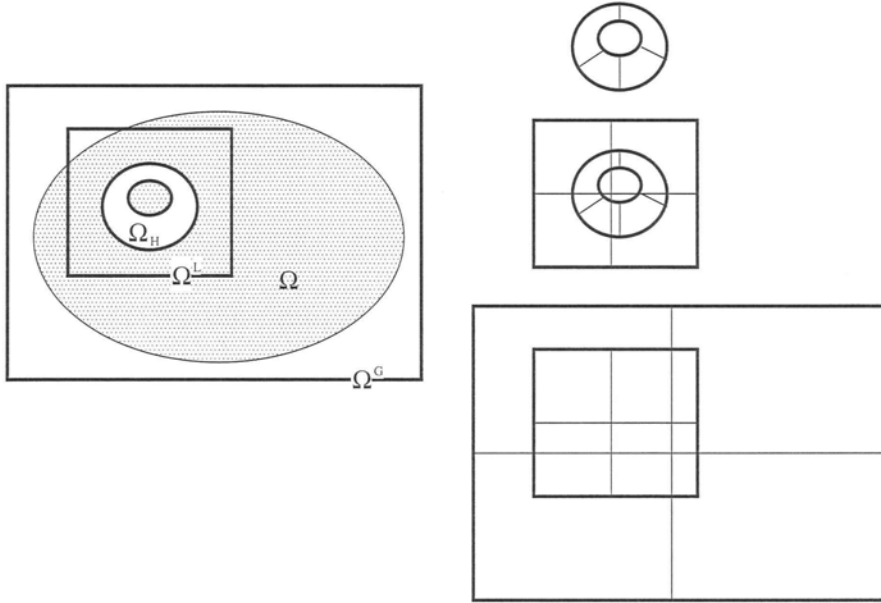
FIG. C.1. *(Left) two-dimensional image of three meshes (Ω_H (on the heart), Ω^L (local rectangular mesh), Ω^G (global rectangular mesh)) and (right) their partitioning (for 4 processes).*

each phase change are described in the diagram below.

$$(\text{C.1}) \qquad \begin{array}{ccc} & \Omega_H & \\ \phi^L & \updownarrow & K_{\mathrm{i}} V_{\mathrm{m}} \\ & \Omega^L & \\ \phi^G - \hat{\phi}^G & \updownarrow & I_G^{L^T} r^L, \hat{I}_G^L \phi^L \\ & \Omega^G & \end{array}$$

The communication speed of the redistribution between the local and global meshes is crucial to the overall parallel performance because this redistribution is performed every cycle in the local-global multigrid algorithm. The overhead cost for the redistribution in the real-life application has been presented in section 4.

In each phase, parallelism is obtained in a standard way except for the IC smoother in the second and third phases. The IC smoother is modified, as it can easily be parallelized under the regular partitioning; that is, the local IC smoother is performed in each processor with one layer overlap at the subdomain boundaries.

In the case where the Purkinje fiber network is connected, the vectors ϕ_{r}, g_{r} and the matrices K_{sr}, K_{rs}, K_{rr} in (3.14) are stored in one of the processors (say, Proc0), while the matrix for the interpolation on the shared nodes I^{s} is distributed along the regular partitioning of the voxel mesh. Thus, the vector data $K_{\mathrm{sr}}\phi_{\mathrm{r}}^{(k)}$ on Proc0 is scattered in (3.15), and the distributed vector data $I^{\mathrm{s}}\phi^{(k+1)}$ is gathered to Proc0 in (3.18). This process may generate considerable overhead when the number of shared nodes is large.

M.D.) for their support in constructing the heart muscle and torso models and for their useful suggestions in improving the accuracy of the simulation. They would like to thank H. Koga for his great contribution in constructing the Purkinje fiber network model. Finally, they would also like to thank C. W. Oosterlee, Ph.D., for reading the manuscript and for the useful comments.

REFERENCES

[1] D. BAI AND A. BRANDT, *Local mesh refinement multilevel techniques*, SIAM J. Sci. Statist. Comput., 8 (1987), pp. 109–134.

[2] A. BRANDT, *Multi-level adaptive solutions to boundary-value problems*, Math. Comp., 31 (1977), pp. 333–390.

[3] A. BRANDT AND V. MIKULINSKY, *On recombining iterants in multigrid algorithms and problems with small islands*, SIAM J. Sci. Comput., 16 (1995), pp. 20–28.

[4] E. M. CHERRY, H. S. GREENSIDE, AND C. S. HENRIQUEZ, *Efficient simulation of three-dimensional anisotropic cardiac tissue using an adaptive mesh refinement method*, CHAOS, 13 (2003), pp. 853–865.

[5] M. COURTEMANCHE, R. J. RAMIREZ, AND S. NATTEL, *Ionic mechanisms underlying human atrial action potential properties: Insights from a mathematical model*, Amer. J. Physiol., 275 (2003), pp. H301–H321.

[6] D. DiFRANCESCO AND D. NOBLE, *A model of cardiac electrical activity incorporating ionic pumps and concentration changes*, Philos. Trans. R. Soc. Lond. Ser. B, 307 (1985), pp. 353–398.

[7] D. DURRER, R. TH. VAN DAM, G. E. FREUD, M. J. JANSE, F. L. MEIJLER, AND R. C. ARZBAECHER, *Total excitation of the isolated human heart*, Circulation, 41 (1970), pp. 899–912.

[8] D. A. HOOKS, K. A. TOMLINSON, S. G. MARSDEN, I. J. LeGRICE, B. H. SMAILL, A. J. PULLAN, AND P. J. HUNTER, *Cardiac microstructure: Implications for electrical propagation and defibrillation in the heart*, Circ. Res., 91 (2002), pp. 331–338.

[9] G. KARYPIS, K. SCHLOEGEL, AND V. KUMAR, *ParMETIS*, http://www-users.cs.umn.edu/karypis/metis/parmetis/.

[10] M. W. KROLL AND M. H. LEHMANN, *Implantable Cardioverter Defibrillator Therapy*, Kluwer Academic, Norwell, MA, 1996.

[11] CH. LUO AND Y. RUDY, *A model of the ventricular cardiac action potential. Depolarization, repolarization, and their interaction*, Circ. Res., 68 (1991), pp. 1501–1526.

[12] S. F. McCORMICK, *Multilevel Adaptive Methods for Partial Differential Equations*, Frontiers Appl. Math. 6, SIAM, Philadelphia, 1989.

[13] C. MENDEZ, W. J. MUELLER, AND X. URGUIAGA, *Propagation of impulses across the Purkinje fiber-muscle junctions in the dog heart*, Circ. Res., 26 (1970), pp. 135–150.

[14] M. PENNACCHIO, *The mortar finite element method for the cardiac bidomain model of extracellular potential*, J. Sci. Comput., 20 (2004), pp. 191–210.

[15] G. PLANK, M. LIEBMANN, R. WEBER DOS SANTOS, E. J. VIGMOND, AND G. HASSE, *Algebraic multigrid preconditioner for the cardiac bidomain model*, IEEE Trans. Biomed. Engrg., 54 (2007), pp. 585–596.

[16] R. PLONSEY, *Bioelectric sources arising in excitable fibers (ALZA lectures)*, Ann. Biomed. Engrg., 16 (1988), pp. 519–546.

[17] J. SUNDNES, G. T. LINES, K. A. MARDAL, AND A. TVEITO, *Multigrid block preconditioning for a coupled system of partial differential equations modeling the electrical activity in the heart*, Comput. Methods Biomech. Biomed. Engrg., 5 (2002), pp. 397–409.

[18] S. TAWARA, *Das Reitzleitungssystem des Saugetierherzens: Eine anatomisch-histologische Studie uber das Atrioventrikularbundel und die Purkinjeschen Faden*, Gustav Fischer, Jena, Germany, 1906.

[19] K. H. W. J. TEN TUSSCHER, D. NOBLE, P. J. NOBLE, AND A. V. PANFILOV, *A model for human ventricular tissue*, Amer. J. Physiol. Heart Circ. Physiol., 286 (2004), pp. H1573–H1589.

[20] U. TROTTENBERG, C. OOSTERLEE, AND A. SCHÜLLER, *Multigrid*, Academic Press, San Diego, CA, 2001, pp. 356–381.

[21] L. TUNG, *A Bi-domain Model for Describing Ischemic Myocardial D-C Potentials*, Ph.D. Thesis, MIT, Cambridge, MA, 1978.

[22] E. J. VIGMOND AND C. CLEMENTS, *Construction of a computer model to investigate sawtooth effects in the Purkinje system*, IEEE Trans. Biomed. Engrg., 54 (2007), pp. 389–399.

[23] E. J. VIGMOND AND L. J. LEON, *Computationally efficient model for simulating electrical activity in cardiac tissue with fiber rotation*, Ann. Biomed. Engrg., 27 (1999), pp. 160–170.

[24] E. J. VIGMOND, F. AGUEL, AND N. A. TRAYANOVA, *Computational techniques for solving the bidomain equation*, IEEE Trans. Biomed. Engrg., 49 (2002), pp. 1260–1269.

[25] *The Visible Human Project*, http://www.nlm.nih.gov/research/visible/visible_human.html.

[26] R. WEBER DOS SANTOS, G. PLANK, S. BAUER, AND E. J. VIGMOND, *Parallel multigrid preconditioner for the cardiac bidomain model*, IEEE Trans. Biomed. Engrg., 51 (2004), pp. 1960–1968.

[27] T. WASHIO AND C. OOSTERLEE, *Error analysis for a potential problem on locally refined grids*, Numer. Math., 86 (2000), pp. 539–563.

[28] T. WASHIO AND C. OOSTERLEE, *Krylov subspace acceleration for nonlinear multigrid schemes*, Electron. Trans. Numer. Anal., 6 (1997), pp. 271–290.

[29] P. WESSELING, *Introduction to Multigrid Methods*, Wiley, Chichester, UK, 1992.

Effects of Wall Stress on the Dynamics of Ventricular Fibrillation: A Simulation Study Using a Dynamic Mechanoelectric Model of Ventricular Tissue

SATOKO HIRABAYASHI, MASTER OF ENVIRONMENT,* MASASHI INAGAKI, M.D.,†
and TOSHIAKI HISADA, PH.D.*

From the *Computational Biomechanics Laboratory, Department of Human and Engineered Environmental Studies, Graduate School of
Frontier Sciences, The University of Tokyo, Tokyo, Japan; and †National Cardiovascular Center Research Institute, Osaka, Japan

A Mechanoelectrical Simulation of VF. *Introduction:* To investigate the mechanisms underlying the increased prevalence of ventricular fibrillation (VF) in the mechanically compromised heart, we developed a fully coupled electromechanical model of the human ventricular myocardium.

Methods and Results: The model formulated the biophysics of specific ionic currents, excitation–contraction coupling, anisotropic nonlinear deformation of the myocardium, and mechanoelectric feedback (MEF) through stretch-activated channels. Our model suggests that sustained stretches shorten the action potential duration (APD) and flatten the electrical restitution curve, whereas stretches applied at the wavefront prolong the APD. Using this model, we examined the effects of mechanical stresses on the dynamics of spiral reentry. The strain distribution during spiral reentry was complex, and a high strain-gradient region was located in the core of the spiral wave. The wavefront around the core was highly stretched, even at lower pressures, resulting in prolongation of the APD and extension of the refractory area in the wavetail. As the left ventricular pressure increased, the stretched area became wider and the refractory area was further extended. The extended refractory area in the wavetail facilitated the wave breakup and meandering of tips through interactions between the wavefront and wavetail.

Conclusions: This simulation study indicates that mechanical loading promotes meandering and wave breaks of spiral reentry through MEF. Mechanical loading under pathological conditions may contribute to the maintenance of VF through these mechanisms. *(J Cardiovasc Electrophysiol, Vol. 19, pp. 730-739, July 2008)*

stretch-activated channel, spiral reentry, excitation–contraction coupling, electrophysiological model, wall stress

Introduction

Ventricular fibrillation (VF) is frequently seen in patients with ventricular dysfunction, ventricular volume or pressure overload, or dyssynergistic ventricular contraction and relaxation.[1,2] Previous studies have shown that ventricular dilatation or stretching increases the inducibility of VF and the defibrillation thresholds.[3,4] Mechanoelectric feedback (MEF), the phenomenon by which electrophysiological changes of the heart are brought about by mechanical changes, is a potential mechanism for these effects and may contribute to lethal ventricular arrhythmias in humans.[5] Recently, Moreno *et al.* examined VF dynamics in animal experiments and reported

that ventricular pressure overload increased the density of singularity points and rotors.[6] However, the precise mechanisms by which mechanical load complicates VF dynamics remain unclear.

Although the development of optical transmembrane potential mapping using voltage-sensitive dyes has enabled us to gain insights into VF dynamics,[7] it is difficult to evaluate the interactions between myocardial strain and electrical activity during VF.[8] Computer simulation is another effective tool for investigating the electrical activity of the heart, and several mechanisms of VF have been proposed on the basis of modeling studies.[9] Some previous simulation studies investigated the role of MEF in arrhythmogenesis.[10,11] However, none of these studies combined the biophysics of specific ionic currents, excitation–contraction coupling, deformation, and MEF.

The present simulation study was undertaken to clarify the fundamental effects of mechanical stresses on the dynamics of spiral waves (SWs). Our hypothesis was that mechanical stresses facilitate meandering and wave breaks of spiral reentry through MEF. To validate this hypothesis, we developed a fully coupled electromechanical model of the human ventricular myocardium. We ran quasi two-dimensional simulations, rather than three-dimensional simulations, because the tissue thickness and rotational anisotropy complicate the dynamics of SWs and make it difficult for us to examine the direct effects of mechanical stresses.

Methods

Mathematical Model

We developed a new mathematical model by combining several existing models as follows: electrophysiological models,[12,13] a stretch-activated channel (SAC) model,[14] an excitation–contraction coupling model,[15] and constitutive equations.[16,17] Here, we only present new definitions or modified values of parameters, and do not show those that remain the same as in the original models.

A mathematical description of wave propagation in cardiac tissue is based on the following equation:[18]

$$C_m \frac{\partial V_m}{\partial t} = -(I_{ion} + I_{stim}) + \frac{1}{S}\nabla_X \cdot (D\nabla_X V_m) \quad (1)$$

where C_m is the membrane capacitance per unit membrane area, V_m is the transmembrane potential, I_{ion} is the total ionic transmembrane current per unit membrane area, I_{stim} is the electric stimulus current per unit membrane area, S is the surface-to-volume ratio, ∇_X is the three-dimensional gradient operator, and D is a tensor of conductivities. Although we used the same values as ten Tusscher *et al.* for C_m and S,[13] we used the following formula for D to reproduce the anisotropy:

$$D = (\sigma_L - \sigma_T)n \otimes n + \sigma_T I \quad (2)$$

where σ_L (= 0.47630 S/m) is the longitudinal conductivity, σ_T (= 0.06348 S/m) is the transverse conductivity, n is a unit vector defining the preferred direction of muscle fibers, and I is the identity tensor. In Equation 1, the divergence and gradient operators are based on the undeformed state. Since the resistances of the cytoplasm and extracellular space are negligible, the conductivity of the tissues depends on the density of gap junctions.[19] Under the assumption that C_m, S, and the resistance of each gap junction do not change with deformation of the tissue, the equation using the transmembrane potential mapped onto the undeformed state is identical to the one using variables in the deformed state.

For the total ionic transmembrane current, I_{ion}, we used the human ventricular cell model formulated by ten Tusscher *et al.*[13] We modified several equations and values and added a stretch-activated current ($I_{stretch}$) as follows. The stretch-activated current was modeled using a nonspecific current with three components (Na⁺-carrying element, K⁺-carrying element, and Ca²⁺-carrying element).

$$I_{stretch} = I_{stNa} + I_{stK} + I_{stCa}$$

Each component was modeled according to the following equation by Kohl *et al.*:[14]

$$I_{stX} = G_{stX}\frac{1}{1 + \exp(-2\gamma(SL - SL_{hst}))}(V_m - E_X) \quad (3)$$

where I_{stX} is the current through SACs for any ion X (Na⁺, K⁺, or Ca²⁺), G_{stX} is the maximal conductance for I_{stX}, SL is the sarcomere length, γ is a user-defined scaling factor, SL_{hst} is the sarcomere length at which half-maximal activation occurs, and E_X is the reversal potential for the ion X. We obtained the SL using the following equation:

$$SL = \alpha_c SL_0 \quad (4)$$

where α_c is the stretch ratio in the muscle fiber direction obtained by a finite element analysis (see Appendix 1) and

SL_0 is the natural sarcomere length. In cases where SACs were inactivated, we kept the SL at SL_0. To reproduce the experimental data of MEF, such as the reversal potential of $I_{stretch}$,[20] the proportion of carrier ions of $I_{stretch}$,[21] and the stretch threshold required to cause ectopic excitation,[22] we adjusted the parameters as follows: $G_{stNa} = 30.0$ S/F, $G_{stK} = 0.544$ S/F, $G_{stCa} = 0.3$ S/F, $SL_{hst} = 2.1$ μm, $\gamma = 14.5$, and $SL_0 = 1.94$ μm. Replacing part of the linear leakage currents by these currents, we reduced the maximum conductance of the linear leakage currents (G_{bNa}, G_{bCa}) as follows: $G_{bNa} = 0.0$ S/F and $G_{bCa} = 0.589$ S/F.

For the generation of contraction force, we adopted the excitation–contraction coupling model formulated by Negroni and Lascano.[15] Using their model, we calculated the concentrations of the following four kinds of ions: free troponin C ([T]), Ca²⁺ bound to troponin C ([TCa]), Ca²⁺ bound to troponin C and attached by cross-bridges ([TCa*]), and troponin C attached by cross-bridges but not associated with Ca²⁺ ([T*]). Since cross-bridges generate contraction forces, we defined the relative force, F, as follows:

$$F = [T^*] + [TCa^*]. \quad (5)$$

We coupled the electrophysiological model with the excitation–contraction coupling model by calculating the free calcium concentration in the cytoplasm (Ca$_i$) as follows. First, by subtracting [TCa] and [TCa*] from the concentration of total calcium in the cytoplasm (Ca$_{i total}$), which was calculated from the electrophysiological model, we obtained the sum of the calcium concentration buffered by calmodulin (buffered[CMDN]) and Ca$_i$ using the following equation:

$$Ca_{i total} = [TCa] + [TCa^*] + buffered[CMDN] + Ca_i. \quad (6)$$

Then, assuming a steady state for buffering reactions by calmodulin, we divided Ca$_i$ and buffered[CMDN] according to the ratio given in the Luo-Rudy dynamic model.[12]

To characterize the properties of cardiac muscles, we adopted the method of Watanabe *et al.*[23] using the Lin-Yin model[16,17] for the constitutive equation. This model is based on the anisotropic hyperelastic material theory, and the strain energy potential, W, is divided into two components, namely the passive component (W_{pass}) and the active component (W_{act}), as follows:

$$W = W_{pass} + W_{act}. \quad (7)$$

$$W_{pass} = c_1(\alpha_c - 1)^2 + c_2(\alpha_c - 1)^3 + c_3(I_1 - 3)$$
$$+ c_4(I_1 - 3)(\alpha_c - 1) + c_5(I_1 - 3)^2, \quad (8)$$

$$W_{act} = C_0 + C_1(I_1 - 3)(I_4 - 1) + C_2(I_1 - 3)^2$$
$$+ C_3(I_4 - 1)^2 + C_4(I_1 - 3) + C_5(I_4 - 1), \quad (9)$$

where I_1 and I_4 are the invariants of the right Cauchy-Green deformation tensor (see Appendix 1), $c_1 = 30.55$ gf/cm², $c_2 = 80.8$ gf/cm², $c_3 = 3.59$ gf/cm², $c_4 = -20.27$ gf/cm², and $c_5 = 30.21$ gf/cm².[17] Following the literature,[23] we treated the coefficients in W_{act} as functions of the relative force, F,

calculated by Equation 5:

$$C_0 = C_{a0}F, \ C_1 = C_{a1}F, \ C_2 = C_{a2}F, \ C_3$$
$$= C_{a3}F, \ C_4 = C_{a4}F^2, \ C_5 = C_{a5}F^2. \quad (10)$$

To reproduce the stress–strain relationships at different Ca_i values obtained from the excitation-contraction coupling model formulated by Negroni and Lascano,[15] we adjusted the coefficients as follows: $C_{a0} = 0.00$ GPa/M, $C_{a1} = -1.60$ GPa/M, $C_{a2} = 4.49$ GPa/M, $C_{a3} = 4.34$ GPa/M, $C_{a4} = 0.476$ GPa/mM^2, and $C_{a5} = 1.21$ GPa/mM^2. We fitted the curves to those obtained with the Ca_i corresponding to each F, that is, $Ca_i = 2.5 \ \mu$M when $F = 15.3 \ \mu$M, $Ca_i = 0.63 \ \mu$M when $F = 6.9 \ \mu$M and $Ca_i = 0.16 \ \mu$M when $F = 1.4 \ \mu$M. The stress–strain relationships at these Fs followed similar patterns to those found experimentally at the corresponding Ca_i values.[24] As F increased, the stress–strain relationship shifted upward and leftward, and became concave. Subsequently, the equilibrium states broke and the muscles deformed. The deformation of muscles was reflected in the SL and changed $I_{stretch}$ as mentioned before.
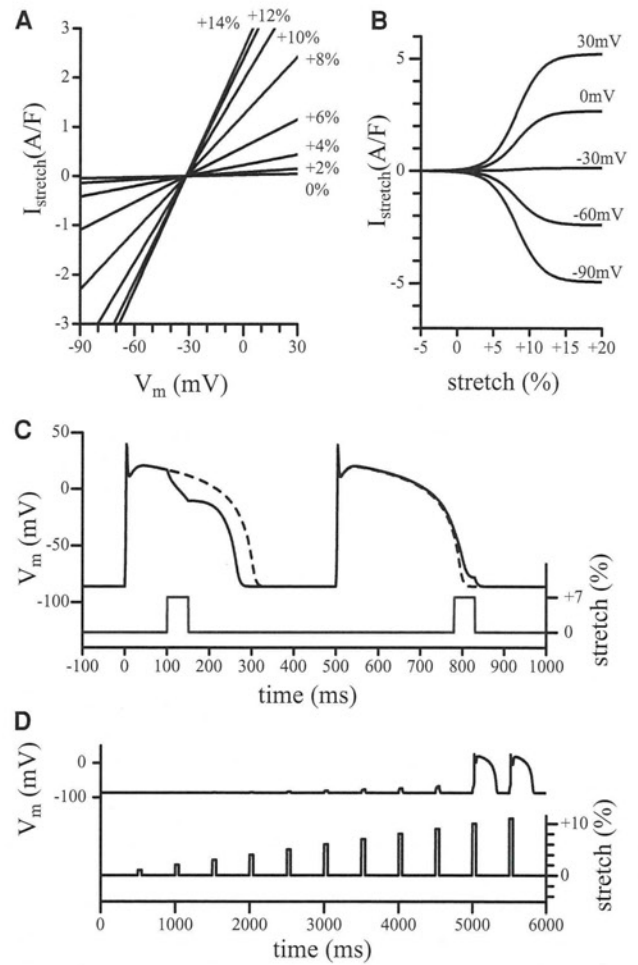
Using a finite element method, we solved Equation 1, the equilibrium equation, and constraints of slight compressibility. We constructed a midmyocardial layer of $75 \times 75 \times 0.2$ mm using 140,625 mixed hexahedral solid elements (eight nodes for the bilinear displacement or transmembrane potential interpolation/constant pressure field). The total amount of freedom is 1,271,633, and the average volume of the finite element is 0.008 mm^3 ($0.2 \times 0.2 \times 0.2$ mm). The total ionic transmembrane current, I_{ion}, was calculated at each node. We developed an efficient dynamic finite element method (see Appendix 2) for computation. By virtue of this method and parallelization, we calculated the whole process from the electrophysiological level to the mechanical level using the same time-step of 0.01 ms.

The Neumann boundary conditions were used for the electric boundary conditions. On the other hand, the mechanical boundary conditions were prescribed from swine experimental data,[25] where the left ventricular (LV) muscle volume was 62 mL and the LV inner volume was 28 mL under unloaded conditions and 38 mL during VF. The LV pressure (LVP) during VF is supposed to be 10 mmHg. Idealizing the LV as a spherical shell, we estimated that the isotropic in-plane strain is about 6% in the midmyocardial layer during VF. Assuming material incompressibility, this in-plane strain indicates that the thickness of the layer is reduced by about 11%. To realize such geometric conditions, we prescribed anisotropic tractions on the side boundary of the midmyocardial layer (Table 1; LVP = 10 mmHg). We prescribed additional tractions corresponding to 6 and 20 mmHg (Table 1), where outward tractions are defined as positive.
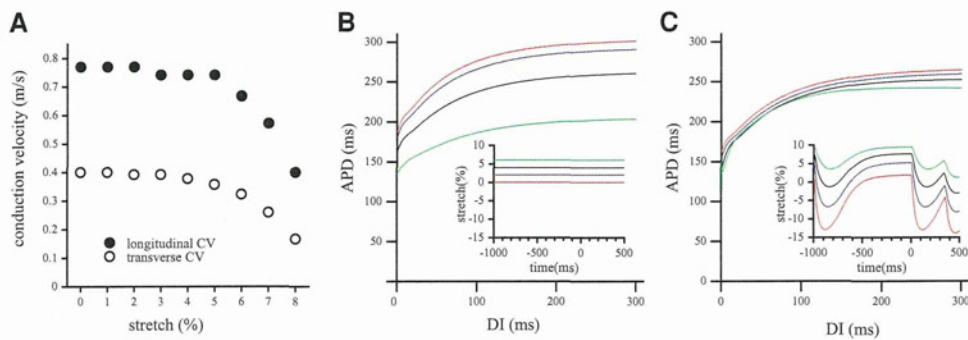

Figure 1. *Basic characteristics of the model. A: Current–voltage relationships of Istretch for 0%, 2%, 4%, 6%, 8%, 10%, 12%, and 14% stretches. All curves were obtained with 11.6 mM [Na$^+$]i, 138.3 mM [K$^+$]i , and 0.0002 mM [Ca^{2+}]i. The reversal potentials are –30 mV for all stretches. B: Current–stretch relationships of $I_{stretch}$ for –90, –60, –30, 0, and 30 mV of transmembrane potentials. C: Phase-dependent effects of stretches on the action potential. The upper line indicates the transmembrane potential and the lower line indicates the stretches. Under 2-Hz pacing, 7% stretches were applied at phase 2 (100–150 ms after the electric stimulus) and phase 3 (280–320 ms after the electric stimulus). Action potentials with no stretches are also shown (dashed line). D: Mechanically induced ectopic excitations. The upper line indicates the transmembrane potential and the lower line indicates the stretches. Stretch pulses (duration 50 ms) were gradually strengthened. Stretches of >10% caused ectopic depolarizations, whereas those of <9% did not.*

Protocols

Giving the midmyocardial layer 6 mmHg of LVP and inactivating the SACs, we induced SWs using the basic pacing stimulus (S1)-premature stimulus (S2) cross-field stimulation protocol. After the SWs stabilized, we activated the SACs and increased LVP by the following protocols: in protocol 1, LVP was kept at 6 mmHg; in protocols 2 and 3, LVP was linearly increased to 10 and 20 mmHg, respectively; in protocol 4, SACs were not activated and LVP was kept at 6 mmHg. We also examined other protocols in which SACs were not activated and LVP was increased to 10 or 20 mmHg. The data for these latter two protocols are not shown because the dynamics of the SWs in these protocols were almost the same as those in protocol 4.

TABLE 1
Boundary In-Plane Stresses Correspond to LVPs

LVP	Along Fiber	Cross-Fiber
6 mmHg	−5 mmHg	−100 mmHg
10 mmHg (Control)	45 mmHg	−120 mmHg
20 mmHg	70 mmHg	−130 mmHg

LVP = left ventricular pressure.

Figure 2. *Effects of stretches on the conduction velocity (CV) and action potential duration (APD). A: Effects of stretches on the CV under 1-Hz pacing. Both the longitudinal and transverse CVs decrease as the stretches increase. B: Effects of constant stretches on the APD restitution curve at a basic pacing cycle length (S1-S1) of 1,000 ms. APD restitution curves were obtained under the 0% (red), 2% (blue), 4% (black), and 6% (green) stretch condition in which the stretch was kept constant. C, APD restitution curves were obtained under dynamic stretch conditions in which the stretches were altered by active tissue contraction. The insets show the histories of the stretches. The last S1 stimuli were applied at time 0. The premature (S2) stimuli were applied after a diastolic interval (DI) of 90 ms.*

Results

Basic Characteristics of the Model

With constant intracellular ion concentrations ($[Na^+]_i =$ 11.6 mM, $[K^+]_i = 138.3$ mM, and $[Ca^{2+}]_i = 0.0002$ mM), $I_{stretch}$ values were calculated for various values of the *SL* and V_m. $I_{stretch}$ was linearly correlated with V_m and the reversal potential of $I_{stretch}$ was −30 mV (Fig. 1A). These results are consistent with experimental data.[20] The amplitude of $I_{stretch}$ increased with stretches and became saturated at around +15% stretch (Fig. 1B). Under constant pacing (2 Hz), we applied stretch pulses at various phases of the action potential. A stretch pulse applied during phase 2 of the action potential resulted in quick repolarization and shortened the action potential duration (APD), whereas a stretch pulse applied at late repolarization (late phase 3 of the action potential) prolonged the APD (Fig. 1C). Figure 1D shows the responses of V_m to a series of stretch pulses (pulse duration 50 ms) of successively increasing amplitudes. The stretch pulses induced transient diastolic membrane depolarizations, which increased in parallel with the increases in the stretch amplitude. Above a certain amplitude (stretch threshold), these stretch-induced depolarizations triggered ectopic excitation. The stretch threshold was 9.5% in this simulation, consistent with the threshold of 9.517% in an experimental study using rectangular pieces of frog heart tissue.[22]

Effects of Stretches on Conduction Velocity and the APD

Figure 2A depicts the relationship between stretches and the conduction velocity (CV) under 1-Hz pacing. We defined the CV as the unstretched length of the tissue excitation propagated in a unit time. Both the longitudinal and transverse CVs decreased with stretches. The electrical restitution curves for various stretches are shown in Figure 2B and C. Under constant stretch conditions (Fig. 2B), the stretches were kept constant. Under dynamic stretch conditions (Fig. 2C), the stretches were estimated from the relative force, *F*, and altered by active tissue contraction. Constant stretches decreased the maximal slope of the restitution curve, while dynamic stretches slightly increased the maximal slope of the restitution curve. Both constant and dynamic stretches shortened the APDs at the plateau of the restitution curve.

Effects of Stretches on SW Dynamics

The electromechanical activities during spiral reentry at 10 mmHg of LVP are illustrated in Figure 3A. As a result of the contraction force generated by the SWs, the strains were irregularly distributed from about −3% to about +10%, despite the homogeneous mechanical boundary conditions. In particular, complex strain distributions were observed around the core of the SW.

Figure 3B shows the transmembrane potential distribution during spiral reentry at various levels of LVP, and the locations of the SW tips are marked with circles. Under the condition in which the SACs were inactivated (SAC[−]), the transmembrane potential distribution had smooth contours for the SW. Under the conditions in which SACs were activated (SAC[+]), the transmembrane potential distribution became irregular as LVP increased. At 20 mmHg of LVP, the SW frequently broke up at several sites of the wavefront, producing new tips, and a single SW became fragmented into a complex pattern of activation. After colliding with each other or against the boundaries, most of the new tips disappeared. However, some tips survived and increased the number of stable tips, as shown in the panel for the 3,435-ms time point. At lower pressures, a meandering SW was sustained, and showed various trajectories of the tip. Figure 4A shows the trajectories of tips under the SAC(−) condition and at LVPs of 6 and 10 mmHg under the SAC(+) condition. The tips drew S-shaped lines, which rotated and drew shapes like a flower. At 6 mmHg of LVP, the trajectory was similar to the one under the SAC(−) condition, where the tip moved between dotted lines and the center of the S-shaped lines was stationary on a dashed line. At 10 mmHg, the center of the S-shaped lines drifted toward the right, and the tip moved around a wider area, compared with the SAC(−) condition. The trajectories that divided into S-shaped lines are shown in Figure 4B. The S-shaped lines rotated faster at 10 mmHg than at 6 mmHg. At 10 mmHg, we frequently found a serial process of wave breaks, and mutual annihilation resulted in a switch of trajectories. We have illustrated a typical pattern of this process in Figure 4C. In the left panel, the trajectories of three tips are plotted in *x* and *y* time space. In the right panel, the transmembrane potential distributions during this process are shown. At 2,770 ms, the wavefront of the SW broke up in the vicinity of the core and a pair of new tips (red
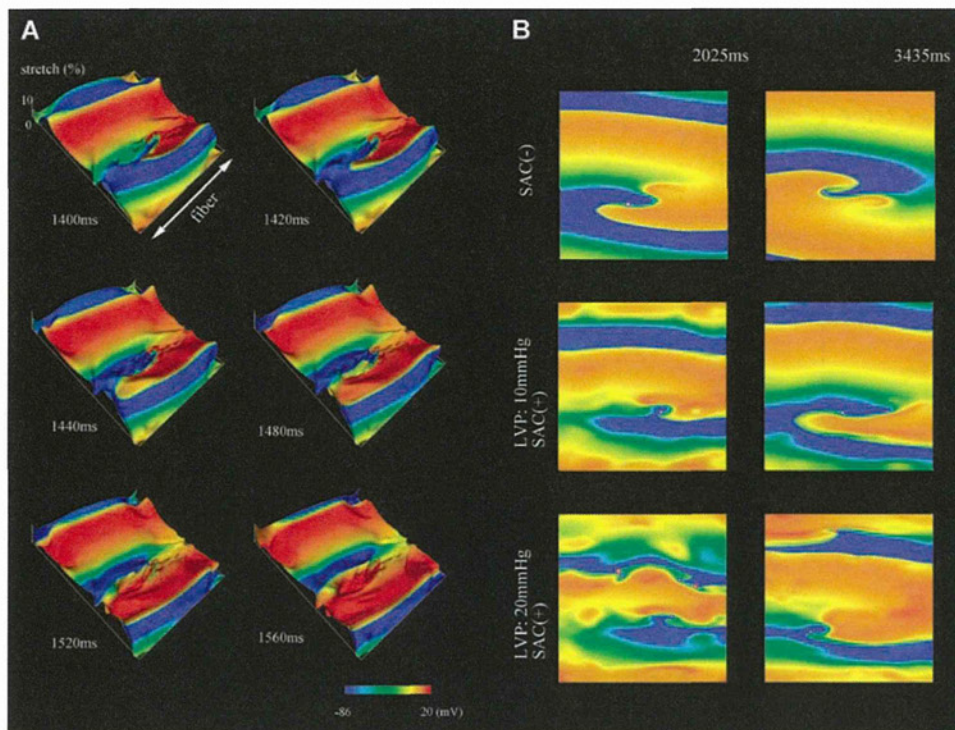
Figure 3. *A: Electromechanical activity during spiral reentry at 10 mmHg of left ventricular pressure (LVP). A time series of transmembrane potential distributions (colors) and strain distributions (heights) is shown. Complex strain distributions can be observed around the core of the spiral waves (SW). B: Transmembrane potential patterns during spiral reentry at stretch-activated channel (SAC)(–), 10 mmHg of LVP and 20 mmHg of LVP. The locations of tips are marked with circles. A blue circle denotes a tip with clockwise rotation of the activation wavefront, whereas a red circle denotes a tip with counterclockwise rotation of the activation wavefront. In the SAC(–) condition, the SW has smooth contours. In the SAC(+) condition, the contours become irregular as the pressure increases.*

and blue) was generated. One of the new tips (red) and an old tip (green) came close to each other. At 2,794 ms, the red tip collided with the green tip, resulting in mutual annihilation. The blue tip survived and traced a new trajectory. This series of processes was observed twice in every S-shaped line marked by a single asterisk, and once in every S-shaped line marked by two asterisks in Figure 4B.

A time series of the distribution of transmembrane potentials and strains at 10 mmHg is shown in Figure 5A, where the contracted area is covered with white. This figure depicts the process by which the wavefront broke up and a pair of new tips was generated (2,770 ms). The myocardium around the core was stretched at phase 0 of the action potential and at late recovery, as shown in Figure 5B, which contains the histories of the V_m and the strain recorded at the point corresponding to the asterisk in Figure 5A. Stretches at these time points prolonged the APD and allowed the SW wavefront to hit the wavetail, resulting in a wave break in the vicinity of the core. In cases in which the APD prolongation was insufficient to generate a wave break, the tip traced the boundary of the enlarged refractory area and the bend of the S-shaped line was sharpened (Fig. 5C).

Discussion

We have conducted simulations of the effects of mechanical stresses on SW dynamics. The electrical activity and deformation during spiral reentry were simulated using a fully coupled electromechanical model of the myocardium. The strain distribution during spiral reentry was complex, and a

high strain-gradient region was located in the core of the SW. Pressure overload promoted meandering and wave breaks of spiral reentry through MEF.

Electromechanical Model of the Myocardium

In the present study, we have proposed a new mathematical model of the human ventricular myocardium that couples all the processes of electrical activity, excitation–contraction coupling, deformation, and MEF. A number of simulation studies have investigated the effects of electrical activity on myocardial contraction using various models of excitation–contraction coupling.[26,27] However, these studies did not account for the effects of MEF. On the other hand, simulation studies that investigated the effects of myocardial deformation on electrical activity did not account for the effects of excitation–contraction coupling.[10,28] Recently, Nash and Panfilov reported a framework for studying the combined effects of cardiac mechanics and electrical activities during arrhythmia.[11] However, their study used a simple FitzHugh-Nagumo type model, and many biological details were absent.

Our model includes detailed biological processes and enables us to investigate the effects of specific biological processes on arrhythmogenesis. Our model quantitatively reproduced the features of MEF, such as the reversal potential of $I_{stretch}$ and the stretch threshold required to induce ectopic excitation. To achieve this, we employed the following parameters: $G_{stNa} = 30.0$ S/F, $G_{stK} = 0.544$ S/F, and $G_{stCa} = 0.3$ S/F. These parameters indicate that Na$^+$ is the main carrier
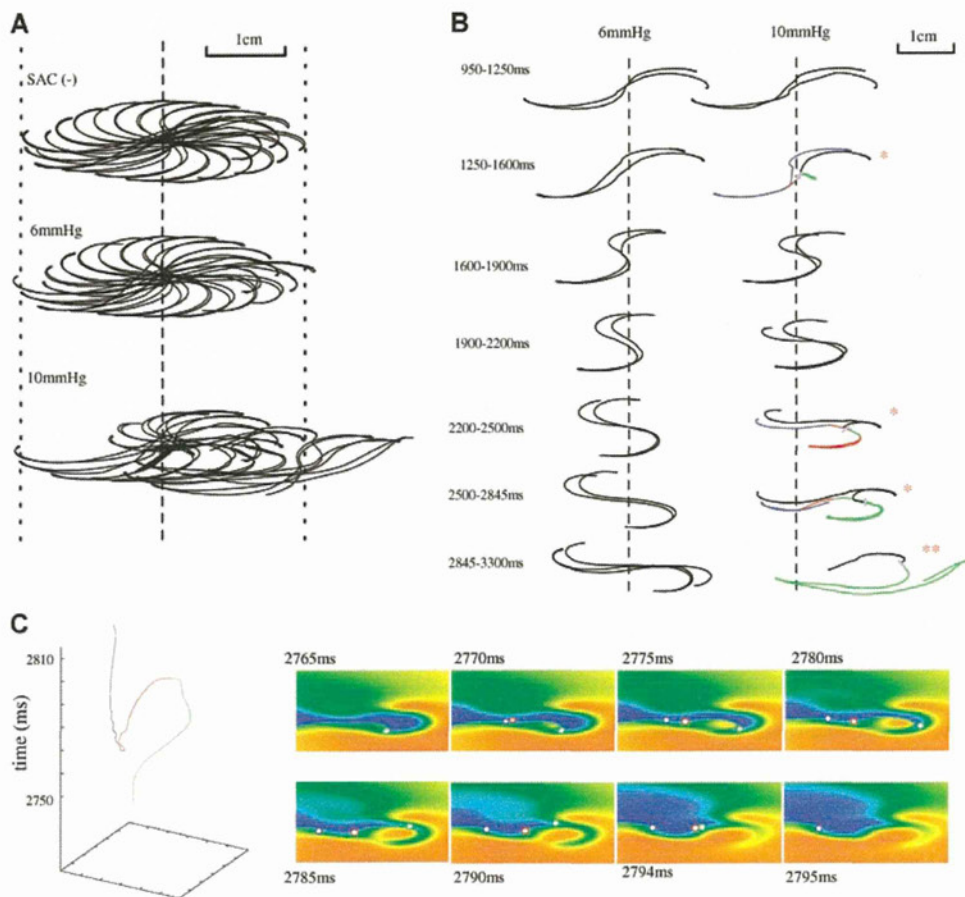
Figure 4. *Dynamics of spiral waves (SW) tips. A: Trajectories of SW tips from 600 to 4,000 ms under SAC(–), 6 mmHg of left ventricular pressure (LVP) and 10 mmHg of LVP. B: Time series of S-shaped lines at 6 and 10 mmHg of LVP. At 10 mmHg, switches of the trajectories are frequently observed. Colored lines indicate the new trajectories. Double switches are observed in the S-shaped trajectories marked by single asterisks, while single switches are observed in S-shaped trajectories marked by two asterisks. C: Typical switching process of tips. The trajectories of three tips are shown on the left. The colors correspond to those in the right-hand figures, which show the transmembrane potential patterns near the core. After a pair of new tips (red and blue) is generated, one of the new tips (red) collides with an old tip (green), resulting in mutual annihilation. The other new tip (blue) survives and traces a new trajectory.*

of $I_{stretch}$ and that Ca^{2+} does not act as a significant carrier, as reported in an experimental study.[21]

Effects of Stretches on the CV and APD

Our calculated values for CVs under unstressed conditions are consistent with the CVs reported in a clinical study.[29] We found that severe stretches decreased the longitudinal and transverse CVs, whereas mild stretches minimally affected these CVs. These results are in concordance with the findings of previous experimental studies.[30,31] Using optical transmembrane potential mapping in the isolated rabbit heart, Sung *et al.* found a decrease in the CV when the LV was loaded to 30 mmHg ($\approx+4\%$ stretch in the longitudinal direction and $\approx+3.2\%$ stretch in the transverse direction).[32] The decrease in CV with LV loading was not significantly affected by the nonspecific SAC blocker, streptomycin, suggesting that SACs are unlikely to play a primary role in this effect. Our findings also suggest that mild stretches ($\leq+4\%$) minimally affect the CV through SACs.

Shortening of the APD and effective refractory period (ERP) with mechanical loading has been reported in various species, including rabbits,[31] dogs,[33,34] and humans.[35] However, some investigators have reported prolongation of the APD durin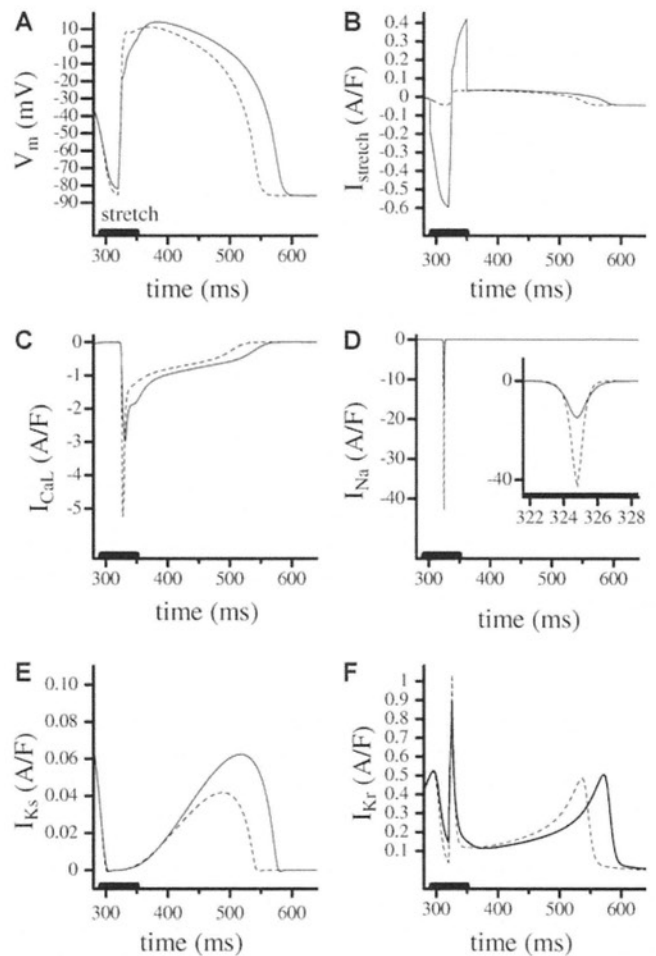g stretches.[32] The manner in which stretches affect the APD is the result of the balance among several competing effects, including SACs and a length-dependent modulation of intracellular calcium handling. Therefore, the effects of stretches on the APD depend on the timing, duration, and intensity of the stretches, which are determined by the conditions of the experimental preparation. We found that stretches applied during phase 2 shortened the APD, while stretches applied during late repolarization prolonged the APD. These results are consistent with the findings of previous experimental[36] and mathematical[14] studies.

Horner *et al.* reported that transient aortic occlusion reduced the APD at the plateau of the restitution curve and increased the maximal slope of the electrical restitution curve in swine hearts.[37] We also found that dynamic stretches increased the maximal slope of the APD restitution curve in our simulation. However, the increase in the maximal slope was small and may not be sufficient to induce frequent wave breaks of SWs. On the other hand, the strains were irregularly distributed during spiral reentry (Fig. 3A) and some myocardial tissue was strongly stretched at the wavefronts of SWs. To examine the effects of stretches at the wavefronts on the action potentials and ionic currents, we applied stretch pulses during a restitution protocol. In Figure 6, a S2 was delivered at 320 ms after the last S1 and a 5% stretch pulse (pulse width 60 ms) was applied at 290 ms after the last S1. Stretches applied

A

B

C
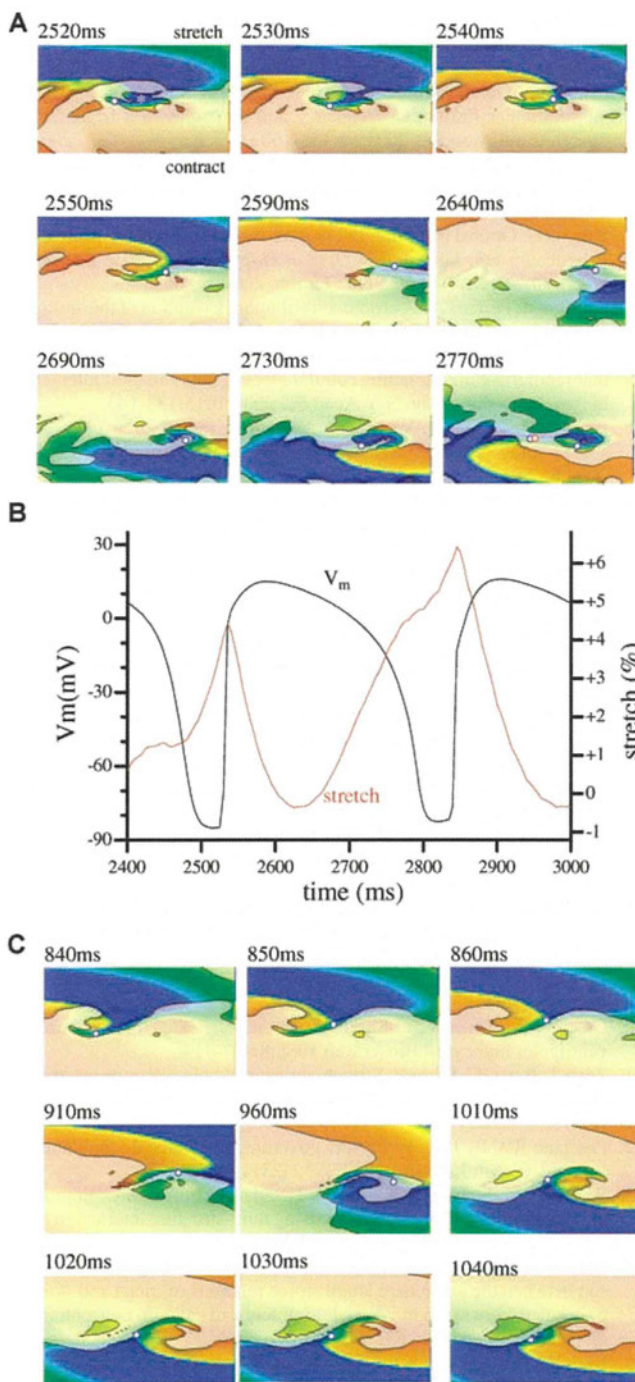
Figure 5. *A, C: Transmembrane potentials and strain distributions during spiral reentry at 10 mmHg of left ventricular pressure (LVP). Colors indicate transmembrane potentials, and contracted areas (strains of <1%) are covered with white. B: Time series of transmembrane potentials and strains recorded at the asterisk in (A).*

Figure 6. *Diastolic stretch-induced changes in ion currents and transmembrane potentials. A premature electric stimulus (S2) was delivered at 320 ms after a basic pacing cycle length (S1-S1) of 1,000 ms. A 5% stretch pulse (solid bar) was applied at 290–350 ms after S1. Values were computed with (solid lines) and without (dashed lines) a stretch pulse. A: Transmembrane potential. B: Stretch-activated current. C: L-type Ca^{2+} current. D: Fast Na^{+} current. E: Slow delayed rectifier potassium current. F: Rapid delayed rectifier potassium current.*

0 and 1 also altered the intensities and kinetics of other ionic currents, including I_{Kr} and I_{Ks}. The decrease in I_{Kr} and increase in I_{Ca-L} during phase 2 augmented the amplitude of the dome and delayed repolarization, resulting in prolongation of the APD. During VF, irregularly distributed strains at the wavefronts would prolong APD inhomogeneously and induce wave breaks of SWs. In heart failure, previous studies[38] have shown that alterations in various ionic currents, including the late sodium current (I_{NaL}),[39] predispose the myocardium to APD prolongation. In addition to action potential modulation, an increase in I_{NaL} in heart failure would lead to diastolic Ca^{2+} overload and modify the strain distribution during VF. These changes may act synergistically with mechanical stresses and facilitate the development and maintenance of VF in heart failure. Experimental studies are required to verify these hypotheses.

Effects of Stretches on SW Dynamics

Around the core of a SW, the stretched region and contracted region were adjacent to each other in a small area. The

during the diastolic phase depolarized the resting membrane potential and decreased the inward Na^{+} current (I_{Na}), thereby resulting in decreases in the amplitudes of phases 0 and 1. The termination of phases 0 and 1 at more negative potentials diminished the availability of the L-type Ca^{2+} current (I_{Ca-L}) and slowed the emergence of the phase 2 dome. Although SAC currents were increased by stretches during phases 0 and 1, the changes in these currents were much smaller than those in I_{Na} and I_{Ca-L}. Decreases in the amplitudes of phases